Fault Diagnosis and Initial Alignment of Redundant SINS Under Large Misalignment Angle

Zeyuan Xu, Xiaohua Zhang, Liang Zhang, Yangguang Xie, Zhiwen Chen, and Danwei Wang, *Life Fellow, IEEE*

***Abstract*—This paper investigates an integrated approach of fault diagnosis and initial alignment of redundant strapdown inertial navigation systems (SINSs) under large misalignment angles. A redundant configuration of four hemispherical resonator gyroscopes (HRGs) and four accelerometers is designed. The parity vector method combined with generalized likelihood ratio test (GLRT) is developed for reliable detection and identification of HRG bias faults. For initial alignment, an analytic coarse alignment provides an initial attitude estimate, which is followed by a precise alignment phase using an unscented Kalman filter (UKF). The UKF is specifically designed to handle the nonlinear error model associated with large yaw misalignment angles. Experimental results demonstrate that the proposed fault diagnosis method effectively identifies HRG faults. Furthermore, comparative studies show that while the UKF and extended Kalman filter (EKF) yield similar performance for small misalignment angles, the UKF achieves significantly superior alignment accuracy, especially under large yaw misalignment angle. This integrated approach enhances system reliability and navigation precision, which achieves a 100% detection rate for the tested bias faults and reduces the yaw error from 20° to below 0.35°.**

***Index Terms*—Fault diagnosis, initial alignment, large misalignment angle, redundant configuration, SINS.**

I. Introduction

STRAPDOWN inertial navigation systems (SINSs) have a wide range of applications, including aerospace [1], [2], marine [3], national defense [4], autonomous vehicles and robots [5], as well as surveying and agriculture [6]. SINS uses gyroscopes and accelerometers to measure the angular velocity and acceleration of objects, and performs positioning, velocity, and attitude calculations independently of external signals [7]–[9]. It is often integrated with satellite navigation and positioning systems, geomagnetism, odometry, and other technologies to improve accuracy and reliability [10], [11]. The factors that limit the performance of SINS are not only inertial sensors (gyroscopes and accelerometers) but also system level errors including the initial alignment error of SINS [12], [13]. In SINS, the initial alignment goal is to accurately determine the attitude matrix (i.e. pitch, roll, and yaw angles) of the carrier coordinate system relative to the navigation coordinate system (usually the local geographic coordinate system).

When there is a significant attitude error (usually defined as a horizontal attitude angle error greater than a few degrees and an yaw angle error greater than 10 degrees) during the initial alignment process, it is called a large misalignment angle [14]. The main reasons for causing large misalignment angles include inertial sensor errors, alignment algorithm defects, external environmental interferences, and installation errors, where the first two can be seen as the internal roots, while the latter two can be seen as external triggers [15]. Thus, as internal roots, inertial sensor errors and alignment algorithm defects should be analyzed and addressed with emphasis. Zero bias is the most common and easily caused factor in inertial sensor errors [16], among which accelerometer zero bias is the main factor causing horizontal misalignment angle (pitch, roll) and gyroscope zero bias is the main factor causing yaw misalignment angle. For example, the constant zero bias of a northbound accelerometer may be mistaken by SINS as a component of gravity in the northbound direction, which results in an incorrect calculation of a northbound inclination angle [17]. When aligning on a static base, the constant zero bias of an eastward gyroscope can be mistaken by SINS as the eastward component of the Earth's rotational angular velocity, which leads to the estimation error of the yaw angle [17]. Therefore, it is necessary to perform fault diagnosis of inertial sensors and eliminate the error sources that cause misalignment angle problems in hardware.

In addition to the zero bias of inertial sensors, the filter used to process alignment algorithms is no longer applicable, which is also an important factor causing large misalignment angles. Model failure under large misalignment angles: alignment algorithms based on classic linear Kalman filter are typically based on the assumption of small angles (small misalignment angle models) [18]. When the initial attitude error is large (i.e. large misalignment angle), these linear models are no longer applicable, and using them can cause the filter to diverge or converge to the wrong state, resulting in larger misalignment angles [19]. Initial alignment is divided into

Received 27 October 2025; revised 4 February 2026; accepted 2 March 2026. This work was supported in part by the European Union's Horizon Europe Program for Marie Skłodowska-Curie Actions (FEASIBLE) under Grant 101149415, the State Key Laboratory of Micro-Spacecraft Rapid Design and Intelligent Cluster under Grant MS01240110, the National Natural Science Foundation of China under Grant 62303002, and the Key Program of Natural Science Foundation of Anhui Higher Education Institutions of China under Grant 2022AH050068. (Corresponding authors: Xiaohua Zhang)

Zeyuan Xu is with the Department of Electrical, Computer and Biomedical Engineering, University of Pavia, 27100 Pavia, Italy (e-mail: zeyuan.xu@unipv.it).

Xiaohua Zhang is with the Nanyang Technological University, 639798, Singapore (e-mail: xiaohua.zhang@ntu.edu.sg).

Liang Zhang is with the School of Electrical Engineering and Automation, Anhui University, Hefei 230093, China (email: liangzhang@ahu.edu.cn).

Yangguang Xie is with the Flight Automatic Control Research Institute, Aviation Industry Corporation of China, Xi'an 710065, China (e-mail: 618gdb104@facri.com).

Zhiwen Chen is with the School of Automation, Central South University, Changsha 410083, China (e-mail: zhiwen.chen@csu.edu.cn).

Danwei Wang is with the School of Electrical and Electronic Engineering, Nanyang Technological University, 639798, Singapore (e-mail: edwwang@ntu.edu.sg).

static-base initial alignment and moving-base initial alignment. Given that there have been many studies on the moving-base initial alignment [20], the static-base initial alignment is investigated. Thus, the static-base initial alignment technology has evolved into a competition for nonlinear filter performance so far [8]. The most representative filters applied to the static-base initial alignment include extended Kalman filter (EKF) [21], unscented Kalman filter (UKF) [22], cubature Kalman filter (CKF) [23], Gaussian-Hermitian filter (GHF) [24], center difference filter (CDF) [25], etc. Nonlinear filters based on Gaussian assumptions are widely used in initial alignment, especially EKF and UKF, due to their low computational complexity and high filtering accuracy. Therefore, these two filters can continue to be applied to further explore their performance under large misalignment angles.

Motivated by the aforementioned studies, this paper presents an integrated framework of gyroscope fault diagnosis and initial alignment for redundant SINSs under large misalignment angles, where the key innovations are below. For fault diagnosis, a new method combining parity-space GLRT fault diagnosis with the design for the redundant HRG configuration is developed to effectively detect and identify HRG bias faults and enhance system reliability. For initial alignment, a phased alignment method is proposed specifically for large misalignment angles, consisting of a coarse alignment phase and a UKF-based precise alignment phase. The performance of the proposed integrated framework is validated through comparative experiments.

II. Design and Fault Diagnosis of Redundant SINS

This section designs a redundant SINS with four HRGs and four accelerometers to enhance system reliability and also proposes a fault detection and identification method for HRGs to achieve the gyroscope fault diagnosis.

A. Design of a Redundant SINS

The signal processing of a redundant SINS is shown in Fig. 1. Firstly, the redundant SINS require A/D conversion of four HRG outputs and four accelerometer outputs. To minimize the phase delay of eight analog signals, a higher sampling frequency should be used as much as possible. Then, the output signal of HRGs and accelerometers still has evident noise after primary filtering, and secondary digital filters are adopted. Next, after sensor level and system level calibrations, the outputs are the rotational angular velocity and acceleration of the body coordinate system relative to the inertial coordinate system. Finally, after initial alignment and fault diagnosis of inertial sensors, strapdown calculation is carried out and then integrated with other navigation systems. It can be seen that fault diagnosis and initial alignment are essential for an SINS.

In this paper, the large misalignment angle mainly refers to the large yaw misalignment angle caused by HRGs, assuming that the accelerometers are relatively ideal. The fault problem of HRGs generally refers to jamming, noise, and bias faults, among which the bias fault is the most common and frequent [26]. Thus, this paper focuses on the diagnosis of HRG bias faults. The redundancy technology of inertial sensors mainly solves the problem of fault detection of inertial sensors and achieves the effective operation of an SINS after removing faulty sensors. The configuration scheme of four HRGs and four accelerometers is designed, as shown in Fig. 2. Four HRGs and four accelerometers are arranged on the $O1$, $O2$, $O3$, and $O4$ measurement axes. Among them, $O1$ and $O3$ are in the XOZ plane, $O2$ and $O4$ are in the YOZ plane, and their angles with the Z-axis are all σ. Four HRGs are in the same plane which is perpendicular to the OZ axis. The same applies to four accelerometers.

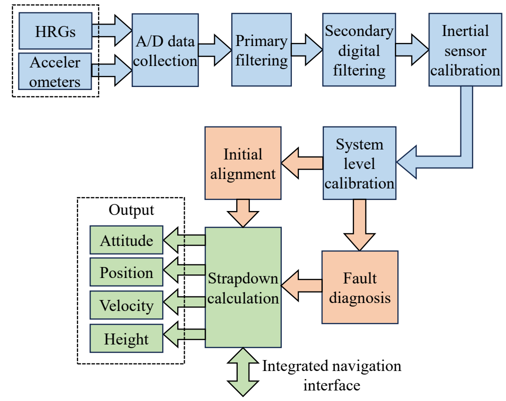

Fig. 1. Signal processing of a redundant SINS.

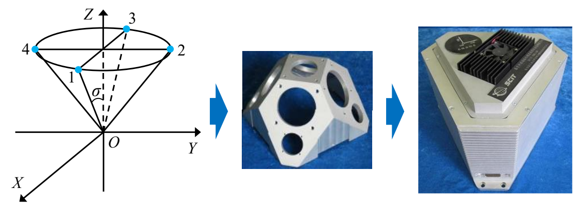

Fig. 2. Configuration scheme of inertial sensors in a redundant SINS.

Regardless of the configuration scheme, the measurement equation of sensors (HRGs [27] and accelerometers) can be written in the following form:

$$\boldsymbol{\Omega} = \boldsymbol{M}\omega + \xi \tag{1}$$

where $\boldsymbol{\Omega}$ and ξ are the output and noise of sensors, respectively, ω denotes angular velocity or specific force to be measured, and $\boldsymbol{M}$ denotes a measurement matrix. The least squares estimate of ω can be obtained from (1) as follows:

$$\hat{\omega} = (\boldsymbol{M}^{\mathrm{T}}\boldsymbol{M})^{-1}\boldsymbol{M}^{\mathrm{T}}\boldsymbol{\Omega} \tag{2}$$

To minimize the impact of individual HRG noise ξ on the least-squares estimate $\hat{\omega}$, σ is designed as $54.735°$ such that the angle between any HRG axis and each coordinate axis is the same [28]. If the ith sensor fails, the ith row of $\boldsymbol{M}$ and the ith element of $\boldsymbol{\Omega}$ are reset or removed to form a new $\boldsymbol{M}$ and $\boldsymbol{\Omega}$. When in the jth fault mode, it is denoted as $\boldsymbol{M}_j$ and $\boldsymbol{\Omega}_j$:

$$\hat{\omega} = (\boldsymbol{M}_j{}^{\mathrm{T}}\boldsymbol{M}_j)^{-1}\boldsymbol{M}_j{}^{\mathrm{T}}\boldsymbol{\Omega}_j = \mathcal{M}_j\boldsymbol{\Omega}_j \tag{3}$$

where $\mathcal{M}_j = (\boldsymbol{M}_j{}^{\mathrm{T}}\boldsymbol{M}_j)^{-1}\boldsymbol{M}_j{}^{\mathrm{T}}$ ($j = 0, 1, \ldots, J-1$), in which J is the number of fault mode, and $j = 0$ indicates no fault. The configuration scheme corresponds one-to-one with $\boldsymbol{M}$, and the optimization of the configuration scheme is the optimization of $\boldsymbol{M}$.

B. Fault Diagnosis of HRGs

The fault detection and identification function of the redundant SINS is analyzed when one of HRGs fails, using the parity vector method. A parity vector is a linear combination of sensor outputs that is independent of a data vector [29]. When there is no fault, it is only a function of noise; when there is a fault, it deviates from a normal value. Based on this characteristic, faults can be detected and identified [5]. Let the parity vector be:

$$\boldsymbol{T} = \boldsymbol{S\Omega} \tag{4}$$

where $\boldsymbol{S} \in \mathbb{R}^{r\times n}$ is a singular matrix and $\boldsymbol{T} \in \mathbb{R}^{r}$. When there is no fault, $\boldsymbol{T} = \boldsymbol{SM}\omega + \boldsymbol{S}\xi$, to make $\boldsymbol{T}$ independent of ω, it is necessary to make

$$\boldsymbol{SM} = 0 \tag{5}$$

Since $\mathrm{rank}(\boldsymbol{M}) = 3$, there are $n-3$ linearly independent rows in $\boldsymbol{S}$, and more linearly correlated rows do not provide more information. Since the smaller r, the smaller the computational complexity, we take

$$r \le n-3 \tag{6}$$

If the ith HRG fails, it can be assumed that there is an additional bias b_i in its output:

$$\boldsymbol{T} = \boldsymbol{S\Omega} = \boldsymbol{S}(\boldsymbol{M}\omega + b_i\boldsymbol{e}_i + \xi) = v_i b_i + \boldsymbol{S}\xi \tag{7}$$

where $\boldsymbol{e}_i$ is an n-dimensional vector with the ith element being 1 and the remaining elements being 0, v_i is the ith column in $\boldsymbol{S}$, and b_i is the fault size (scalar).

To achieve the fault detection of HRGs, a generalized likelihood ratio test (GLRT) approach is developed. Fault detection can be seen as a binary hypothesis testing problem for the parity vector $\boldsymbol{T}$, which can be detected using GLRT approach. By setting $\xi \to N(0, \tau^2 I)$, when there is no fault (F_0):

$$E\{\boldsymbol{T}\} = 0, \mathrm{var}\{\boldsymbol{T}\} = (\boldsymbol{SS}^{\mathrm{T}})\tau^2 \tag{8}$$

when there is a fault (F_f):

$$E\{\boldsymbol{T}\} = \alpha \ne 0, \mathrm{var}\{\boldsymbol{T}\} = (\boldsymbol{SS}^{\mathrm{T}})\tau^2 \tag{9}$$

where α is a chosen false alarm rate (generally selected as 0.27%). Since $\boldsymbol{T}$ is a linear function of ξ, it follows an r-dimensional normal distribution. The likelihood functions for both fault free and fault cases are:

$$\beta(p|\,F_0) = (2\pi)^{-\frac{r}{2}}\left|(\boldsymbol{SS}^{\mathrm{T}})\tau^2\right|^{-\frac{1}{2}} \exp\left[-\tfrac{1}{2\tau^2}\boldsymbol{T}^{\mathrm{T}}(\boldsymbol{SS}^{\mathrm{T}})^{-1}\boldsymbol{T}\right] \tag{10}$$

$$\begin{aligned}\beta(p|\,F_f) = (2\pi)^{-\frac{r}{2}}&\left|(\boldsymbol{SS}^{\mathrm{T}})\tau^2\right|^{-\frac{1}{2}} \\ &\cdot \exp\left[-\tfrac{1}{2\tau^2}(\boldsymbol{T}-\alpha)^{\mathrm{T}}(\boldsymbol{SS}^{\mathrm{T}})^{-1}(\boldsymbol{T}-\alpha)\right]\end{aligned} \tag{11}$$

Thus, the logarithmic likelihood ratio function is

$$\begin{aligned}\Xi(\boldsymbol{T}) &= \ln\left[\tfrac{\beta(p|F_f)}{\beta(p|F_0)}\right] \\ &= \tfrac{1}{2}\left[\boldsymbol{T}^{\mathrm{T}}\tfrac{(\boldsymbol{SS}^{\mathrm{T}})^{-1}}{\tau^2}\boldsymbol{T} - (\boldsymbol{T}-\alpha)^{\mathrm{T}}\tfrac{(\boldsymbol{SS}^{\mathrm{T}})^{-1}}{\tau^2}(\boldsymbol{T}-\alpha)\right]\end{aligned} \tag{12}$$

Regarding the derivative of α in the above equation, the maximum likelihood estimate of α is $\hat{\alpha} = \boldsymbol{T}$, and the maximum likelihood ratio function value is

$$\Xi_{\max}(\boldsymbol{T}) = \tfrac{1}{\tau^2}\boldsymbol{T}^{\mathrm{T}}(\boldsymbol{SS}^{\mathrm{T}})^{-1}\boldsymbol{T} \tag{13}$$

The decision function for fault detection is taken as

$$F_D = \tfrac{1}{2\tau^2}\boldsymbol{T}^{\mathrm{T}}(\boldsymbol{SS}^{\mathrm{T}})^{-1}\boldsymbol{T} \tag{14}$$

If $F_D \le T_D$, there is no fault (F_0); if $F_D > T_D$, there is a fault (F_f). F_D satisfies a χ^2 distribution with degrees of freedom r, specifying the false alarm rate α, and the threshold T_D can be obtained by solving $P(\chi_r^2 > T_D) = \alpha$.

The fault identification of HRGs can be seen as a multivariate hypothesis testing problem, which includes n hypotheses. Using F_i to denote the ith HRG,

$$E\{\boldsymbol{T}\} = v_i b_i, \mathrm{var}\{\boldsymbol{T}\} = (\boldsymbol{SS}^{\mathrm{T}})\tau^2, i = 1, 2, \ldots, n \tag{15}$$

For F_i, the logarithmic likelihood function is

$$\begin{aligned}\ln\left[\beta(p|\,F_i)\right] &= \ln\left[(2\pi)^{-\frac{r}{2}}\left|(\boldsymbol{SS}^{\mathrm{T}})\tau^2\right|^{-\frac{1}{2}}\right] \\ &\quad - \tfrac{1}{2}(\boldsymbol{T}-v_i b_i)^{\mathrm{T}}\tfrac{(\boldsymbol{SS}^{\mathrm{T}})^{-1}}{\tau^2}(\boldsymbol{T}-v_i b_i) \\ &= \ln\left[(2\pi)^{-\frac{r}{2}}\left|(\boldsymbol{SS}^{\mathrm{T}})\tau^2\right|^{-\frac{1}{2}}\right] - \tfrac{1}{2}\left[\left(\boldsymbol{T}^{\mathrm{T}}\tfrac{(\boldsymbol{SS}^{\mathrm{T}})^{-1}}{\tau^2}\boldsymbol{T}\right)\right. \\ &\quad \left. -2b_i\left(\boldsymbol{T}^{\mathrm{T}}\tfrac{(\boldsymbol{SS}^{\mathrm{T}})^{-1}}{\tau^2}v_i\right) + {b_i}^2\left({v_i}^{\mathrm{T}}\tfrac{(\boldsymbol{SS}^{\mathrm{T}})^{-1}}{\tau^2}v_i\right)\right]\end{aligned} \tag{16}$$

Regarding the derivative of b_i in the above equation, the maximum likelihood estimate of b_i is obtained:

$$\hat{b}_i = \frac{\boldsymbol{T}^{\mathrm{T}}(\boldsymbol{SS}^{\mathrm{T}})^{-1}\boldsymbol{T}}{{v_i}^{\mathrm{T}}(\boldsymbol{SS}^{\mathrm{T}})^{-1}v_i} \tag{17}$$

The maximum likelihood estimate is

$$\begin{aligned}\ln\left[\beta(p|\,F_i)\right]_{\max} &= \ln\left[(2\pi)^{-\frac{r}{2}}\left|(\boldsymbol{SS}^{\mathrm{T}})\tau^2\right|^{-\frac{1}{2}}\right] \\ &\quad - \tfrac{1}{2}\boldsymbol{T}^{\mathrm{T}}\tfrac{(\boldsymbol{SS}^{\mathrm{T}})^{-1}}{\tau^2}\boldsymbol{T} + \tfrac{1}{2}\tfrac{\left[\boldsymbol{T}^{\mathrm{T}}(\boldsymbol{SS}^{\mathrm{T}})^{-1}v_i\right]^2}{\tau^2 {v_i}^{\mathrm{T}}(\boldsymbol{SS}^{\mathrm{T}})^{-1}v_i}\end{aligned} \tag{18}$$

The decision function for fault identification is taken as

$$F_{I,i} = \frac{\left[\boldsymbol{T}^{\mathrm{T}}(\boldsymbol{SS}^{\mathrm{T}})^{-1}v_i\right]^2}{\tau^2 {v_i}^{\mathrm{T}}(\boldsymbol{SS}^{\mathrm{T}})^{-1}v_i}, i = 1, 2, \ldots, n \tag{19}$$

When there is a fault, each $F_{I,i}$ is calculated, from which the sequence number of the faulty sensor k can be obtained as $k = \arg\max\{F_{I,i}\}$, where $k \in \{1, 2, \ldots, n\}$.

The most critical issue in using the GLRT method for fault detection and identification is how to construct the singular matrix $\boldsymbol{S}$. According to the definition of parity vector, $\boldsymbol{S}$ must satisfy (5) and the dimensionality must satisfy (6). However, $\boldsymbol{S}$ is not unique. Choosing $\boldsymbol{S}$ reasonably can enhance the ability of fault detection and identification. When a fault occurs, $\boldsymbol{S}$, making $v_i b_i$ in (7) as large as possible, is the optimal parity vector. The optimal solution of $\boldsymbol{S}$ given in [30] satisfies the following equation:

$$\boldsymbol{S}^{\mathrm{T}}(\boldsymbol{SS}^{\mathrm{T}})^{-1}\boldsymbol{S} = \boldsymbol{I} - \boldsymbol{M}(\boldsymbol{M}^{\mathrm{T}}\boldsymbol{M})^{-1}\boldsymbol{M}^{\mathrm{T}} \tag{20}$$

For the configuration scheme in Fig. 2, by combining with (5), (6), and (20), we can obtain $\boldsymbol{S} = \begin{bmatrix} 0.5 & -0.5 & 0.5 & -0.5 \end{bmatrix}$.

Remark 1: The fault diagnosis method based on wavelet transform is also a popular sensor fault diagnosis method currently. The GLRT-parity vector method is specifically designed for redundant sensor configurations. Wavelet transform methods primarily analyze single sensor signal anomalies without leveraging cross-sensor redundancy. While wavelet transform methods are powerful for non-stationary signal analysis, the GLRT-parity vector method is more appropriate for this paper due to its tailored fit with sensor redundancy, statistical fault isolability, model-based rigor, and computational alignment with real-time SINS requirements.

III. Initial Alignment of an SINS

In the section, an analytic coarse alignment offers a rapid initial estimate, which leaves significant yaw errors, and in the subsequent precise alignment phase, an UKF is designed for large yaw misalignment angle cases.

A. Analytic Coarse Alignment

Analytic coarse alignment is to use HRGs and accelerometers measure the Earth's rotational angular velocity and gravity acceleration, and then use the measured values to estimate the value of $\boldsymbol{C}_b^n$, where $\boldsymbol{C}_b^n$ is the transition matrix from the body coordinate system b to the navigation coordinate system n, which provides initial conditions for precise alignment. Specifically, assuming that the local latitude φ is known and the navigation coordinate system n adopts the east-north-sky geographic coordinate system g, the components of the gravitational acceleration g and the Earth's rotational angular velocity ω_{ie} in the navigation coordinate system are determined and known, which can be expressed as

$$\boldsymbol{g}^n = [\ 0 \quad 0 \quad -g]^{\mathrm{T}} \tag{21}$$

$$\boldsymbol{\omega}_{ie}^n =[\ 0 \quad \omega_{ie}\cos L \quad \omega_{ie}\sin L]^{\mathrm{T}} \tag{22}$$

where L is a local geographic latitude. Analytic coarse alignment is to estimate $\boldsymbol{C}_b^n$ using known $\boldsymbol{g}^n$, $\boldsymbol{\omega}_{ie}^n$, and their measured values. In this paper, a method of directly calculating $\boldsymbol{C}_b^n$ using the measured values is adopted to avoid triangle function operations and orthogonalization processes in other calculating methods, which is more suitable for practical engineering applications. Thus,

$$\boldsymbol{C}_b^n = [\ \boldsymbol{x} \quad \boldsymbol{y} \quad \boldsymbol{z}\ ] \tag{23}$$

where $\boldsymbol{x}$, $\boldsymbol{y}$, and $\boldsymbol{z}$ are the three column vectors of $\boldsymbol{C}_b^n$, and they have orthogonal constraints on each other.

By considering measurement errors, the measured values of HRGs amd accelerometers at time k can be expressed as

$$\boldsymbol{a}^b(k) = -g\boldsymbol{z} + \delta\boldsymbol{a}^b(k) \tag{24}$$

where $\boldsymbol{a}^b(k)$ is the output of accelerometers, and $\delta\boldsymbol{a}^b(k)$ is the measurement error.

$$\boldsymbol{\omega}^b(k) = \boldsymbol{\omega}_{ie}\cos\varphi_y + \boldsymbol{\omega}_{ie}\sin\varphi_z + \delta\boldsymbol{\omega}^b(k) \tag{25}$$

where $\boldsymbol{\omega}^b(k)$ is the output of HRGs, $\delta\boldsymbol{\omega}^b(k)$ is the measurement error; φ_y and φ_z are attitude angles. The three component vectors of $\boldsymbol{C}_b^n$ are estimated using the least squares method under orthogonal constraints:

$$\hat{\boldsymbol{z}} = -\frac{1}{\lambda}\sum\nolimits_{k=1}^{N}\boldsymbol{a}^b(k) \tag{26}$$

$$\hat{\boldsymbol{y}} =\frac{1}{\zeta}\left(\sum\nolimits_{k=1}^{N}\boldsymbol{\omega}^b(k) - \boldsymbol{\theta}\cdot\hat{\boldsymbol{z}}\right) \tag{27}$$

$$\hat{\boldsymbol{x}} = \hat{\boldsymbol{y}}\times\hat{\boldsymbol{z}} = \frac{1}{\zeta}\left(\sum\nolimits_{k=1}^{N}\boldsymbol{\omega}^b(k)\right)\times\hat{\boldsymbol{z}} \tag{28}$$

TABLE I
Test Results of Analytic coarse Alignment

Number	Yaw (°)	Pitch (°)	Roll (°)
Ideal value of first test	0	0	0
Test value of first test	351.8467	−0.0032	−0.0011
Ideal value of second test	20	0	0
Test value of second test	11.3485	−0.0043	−0.0028
Ideal value of third test	40	0	0
Test value of third test	43.9476	−0.0076	−0.0041

where N is the total measurement number,

$$\lambda = \left[\left(\sum\nolimits_{k=1}^{N}\boldsymbol{a}^b(k)\right)^{\mathrm{T}}\left(\sum\nolimits_{k=1}^{N}\boldsymbol{a}^b(k)\right)\right]^{1/2} \tag{29}$$

$$\boldsymbol{\theta} = \frac{1}{\lambda}\left(\sum\nolimits_{k=1}^{N}\boldsymbol{a}^b(k)\right)^{\mathrm{T}}\left(\sum\nolimits_{k=1}^{N}\boldsymbol{\omega}^b(k)\right) \tag{30}$$

$$\zeta = \left[\left(\sum\nolimits_{k=1}^{N}\boldsymbol{\omega}^b(k)\right)^{\mathrm{T}}\left(\sum\nolimits_{k=1}^{N}\boldsymbol{\omega}^b(k)\right) - \boldsymbol{\theta}^2\right]^{1/2} \tag{31}$$

Thus, the estimated value of the strapdown matrix can be written as

$$\hat{\boldsymbol{C}}_b^n = [\ \hat{\boldsymbol{x}} \quad \hat{\boldsymbol{y}} \quad \hat{\boldsymbol{z}}\ ] \tag{32}$$

To test the alignment accuracy of the analytic coarse alignment, the SINS's body coordinate system b is aligned with the geographic coordinate system g, then rotate the celestial axis and measure every $20°$. The initial alignment is carried out using the above steps, where the alignment time of every time is 10 seconds and the repeated test number is three times, and the test results are shown in Table I. It can be seen from the test results that the analytic coarse alignment has the alignment error of $0.008°$ for pitch angle, $0.005°$ for roll angle, and $10°$ for yaw angle.

From the analysis of the coarse alignment results, it can be seen that the yaw angle error is significant. At this point, the linear error model based on a small misalignment angle cannot accurately describe the error propagation characteristics of the inertial navigation system. Using a linear error equation will affect the filtering accuracy. Therefore, this paper adopts a nonlinear filtering method based on a nonlinear error model with large yaw misalignment angle.

B. Unscented Kalman Filter of Precise Alignment

The ideal angular velocity output of an SINS under static-base conditions is zero. However, due to errors in inertial sensors and initial conditions, the angular velocity continuously drifts. The initial alignment of the static base is to adopt angular velocity error as the observation value and utilize filtering techniques to estimate error sources based on the propagation characteristics of system error (error equation). Thus, this is the process of inferring the cause from the results, and the accuracy of the propagation characteristics of error sources and the quality of filter design are the two crucial factors that determine the initial alignment performance.

A stochastic system under nonlinear additive Gaussian noise conditions can be described by a statistical state transition

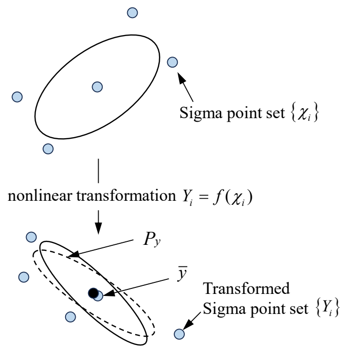

Fig. 3. Transformation of Mean and Covariance for UKF.

equation (discrete) and a statistical measurement equation (discrete):

$$\boldsymbol{X}_k = \boldsymbol{f}(\boldsymbol{X}_{k-1}) + \boldsymbol{U}_{k-1} \tag{33}$$

$$\boldsymbol{Z}_k = \boldsymbol{h}(\boldsymbol{X}_k) + \boldsymbol{V}_k \tag{34}$$

where $\boldsymbol{f}(\cdot)$ denotes an n-dimensional nonlinear vector function of the independent variable $\boldsymbol{X}_{k-1}$, $\boldsymbol{h}(\cdot)$ denotes an m-dimensional nonlinear vector function of the independent variable $\boldsymbol{X}_k$, in which $\boldsymbol{H}_k = \left.\frac{\partial \boldsymbol{h}(\boldsymbol{X})}{\partial \boldsymbol{X}}\right|_{\boldsymbol{X}=\hat{\boldsymbol{X}}_{k|k-1}}$ (this formula is intended only as a conceptual reference to the EKF's linearization step for comparative context), $\boldsymbol{U}_k$ is the dynamic noise of an n-dimensional stochastic system, $\boldsymbol{V}_k$ is the noise of an m-dimensional measurement system, the initial state $\boldsymbol{X}_0$ is usually an n-dimensional random vector of any value, and $\boldsymbol{U}_k$ and $\boldsymbol{V}_k$ are Gaussian white noises, which satisfies:

$$\begin{array}{c} E[\boldsymbol{U}_k] = 0, \mathrm{Cov}[\boldsymbol{U}_k, \boldsymbol{U}_l] = E[\boldsymbol{U}_k \boldsymbol{U}_l^{\mathrm{T}}] = \boldsymbol{Q}_k \delta_{kl} \\ E[\boldsymbol{V}_k] = 0, \mathrm{Cov}[\boldsymbol{V}_k, \boldsymbol{V}_l] = E[\boldsymbol{V}_k \boldsymbol{V}_l^{\mathrm{T}}] = \boldsymbol{R}_k \delta_{kl} \\ \mathrm{Cov}[\boldsymbol{U}_k, \boldsymbol{V}_l] = E[\boldsymbol{U}_k \boldsymbol{V}_l^{\mathrm{T}}] = 0 \end{array} \tag{35}$$

in which $\boldsymbol{Q}_k$ and $\boldsymbol{R}_k$ are the variance matrices of the system noise sequence and the measurement noise sequence, respectively, and both are non-negative matrices.

Given the previous state and all observed values, (33) determines the conditional transition probability for predicting the current state. Also, assuming that the conditional transition probability follows a Gaussian distribution, it is obtained:

$$p\left(\boldsymbol{X}_k \left| \boldsymbol{X}_{k-1}\right., \boldsymbol{Z}_{1:k-1}\right) = N(\boldsymbol{X}_k; \boldsymbol{f}(\boldsymbol{X}_{k-1}), \boldsymbol{Q}_k) \tag{36}$$

where $N(\boldsymbol{X}_k; \boldsymbol{f}(\boldsymbol{X}_{k-1}), \boldsymbol{Q}_k)$ denotes a multi-dimensional normal probability density function with a random vector $\boldsymbol{X}_k$, a mean vector $\boldsymbol{f}(\boldsymbol{X}_{k-1})$, and a variance matrix $\boldsymbol{Q}_k$.

The core idea of UKF is to utilize an unscented transformation to generate a set of determined sampling points (Sigma point set) under the assumption that the state follows a Gaussian distribution and achieve the goal of approximating the probability density distribution of the nonlinear function through nonlinear propagation of the Sigma point set, as shown in Fig. 3.

It is assumed that the random vector $\boldsymbol{X}$ satisfies $\boldsymbol{X} \sim N(\boldsymbol{X}; \bar{\boldsymbol{X}}, \boldsymbol{P}_x)$ and $\boldsymbol{P}_x$ is symmetric and non-negative definite, where $\bar{\boldsymbol{X}}$ is the mean and $\boldsymbol{P}_x$ is the covariance. According to the unscented transformation, the construction method of Sigma point set $\{\boldsymbol{\chi}_i, W_i\}$ is as follows, where W_i is the weight value:

$$\boldsymbol{\chi}_i = \begin{cases} \bar{\boldsymbol{X}}, & i = 0 \\ \bar{\boldsymbol{X}} + \left(\sqrt{(n+\varepsilon)\boldsymbol{P}_x}\right)_i, & i = 1, \ldots, n \\ \bar{\boldsymbol{X}} - \left(\sqrt{(n+\varepsilon)\boldsymbol{P}_x}\right)_i, & i = n+1, \ldots, 2n \end{cases} \tag{37}$$

$$W_i = \begin{cases} \varepsilon/(n+\varepsilon), & i = 0 \\ 1/[2(n+\varepsilon)], & i = 1, \ldots, 2n \end{cases} \tag{38}$$

where ε is a scale parameter that can affect the error caused by high-order moments. The above Sigma point set is propagated through nonlinear functions:

$$\boldsymbol{Y}_i = \boldsymbol{g}(\boldsymbol{\chi}_i), i = 0, 1, \ldots, 2n \tag{39}$$

The mean and variance of $\boldsymbol{Y}$ can be expressed as

$$\bar{\boldsymbol{Y}} \approx \sum_{i=0}^{2n} W_i \boldsymbol{Y}_i \tag{40}$$

$$\boldsymbol{P}_y \approx \sum_{i=0}^{2n} W_i (\boldsymbol{Y}_i - \bar{\boldsymbol{Y}})(\boldsymbol{Y}_i - \bar{\boldsymbol{Y}})^T \tag{41}$$

The mean and variance obtained from Gaussian distribution (40) and (41) can achieve third-order accuracy.

When ε is negative, the above sampling strategy will result in (41) being semi-negative definite. The proportional sampling method can solve this deficiency. The construction method of the Sigma point set is (37) and the new form of (38), where the new form of (38) is:

$$W_i = \begin{cases} W_0^{(m)} = \lambda/(n+\lambda) \\ W_0^{(c)} = \lambda/(n+\lambda) + (1 - \mu^2 + \upsilon) \\ W_i^{(m)} = W_i^{(c)} = 1/[2(n+\lambda)], i = n+1, \cdots, 2n \end{cases} \tag{42}$$

$$\lambda = \mu^2(n+\varepsilon) - n \tag{43}$$

where $W_i^{(m)}$ and $W_i^{(c)}$ are the weighted values of the mean and variance of Sigma points, respectively; μ is a small positive number that determines the distance between Sigma point and $\bar{\boldsymbol{X}}$, usually taken as $1 \times 10^{-4} \leq \mu \leq 1$; υ contains high-order moment information, and the optimal value for Gaussian distribution is $\upsilon = 2$; ε is the second scale parameter, usually taken as 0 or $3 - n$. Using (39) for nonlinear propagation of the new Sigma point set, the mean and variance of $\boldsymbol{Y}$ can be expressed in the following form:

$$\bar{\boldsymbol{Y}} \approx \sum_{i=0}^{2n} W_i^{(m)} \boldsymbol{Y}_i \tag{44}$$

$$\boldsymbol{P}_y \approx \sum_{i=0}^{2n} W_i^{(c)} (\boldsymbol{Y}_i - \bar{\boldsymbol{Y}})(\boldsymbol{Y}_i - \bar{\boldsymbol{Y}})^T \tag{45}$$

The UKF algorithm uses the nonlinear propagation of Sigma point sets to solve the problem of calculating mean and variance integrals in Gaussian filters. For nonlinear discrete systems (33) and (34), the UKF algorithm is shown in Fig. 4. The computational complexity of UKF is of the same order as EKF. The calculation accuracy of UKF for mean and variance can reach second-order accuracy, and can reach third-order accuracy in the case of Gaussian distribution, therefore its accuracy is higher than EKF. In addition, UKF can also be

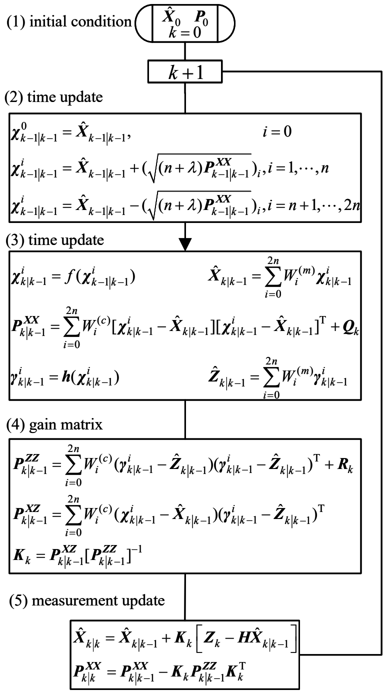

Fig. 4. UKF algorithm.

applied to non-additive noise system equations, with a wider range of applicability than EKF.

Remark 2: The comparative analysis of UKF, CKF, and EKF is below. 1) UKF advantages over CKF: The UKF uses a deterministic sampling approach (sigma points) that captures the mean and covariance more accurately for nonlinear transformations without requiring derivative calculations. It achieves third-order accuracy for Gaussian distributions, while CKF is generally accurate to the second order. This leads to better estimation performance under significant nonlinearities, such as large yaw misalignment. The UKF's scaling parameters allow tuning for different types of nonlinearities, offering flexibility in balancing accuracy and computational load, which is critical in real-time SINS applications. 2) UKF advantages over EKF: The EKF relies on a first-order Taylor series linearization of the system model around the current state estimate. This approximation is valid only under the assumption of small errors. When the initial yaw misalignment is large (e.g., $> 10°$), the neglected higher-order terms become significant, introducing substantial linearization errors that can cause filter divergence, slow convergence, or biased estimates. In contrast, the UKF employs a deterministic sampling approach (the unscented transformation) up to the third order for Gaussian distributions, without ever requiring the derivation of Jacobian matrices. Therefore, while the EKF is sufficient for small misalignment scenarios, the UKF can ensure reliable and precise convergence in the challenging large misalignment alignment task.

IV. Experimental Results

To verify the effectiveness of fault diagnosis and initial alignment methods, an HRG-based redundant SINS system and its testing system are established, as shown in Fig. 5.

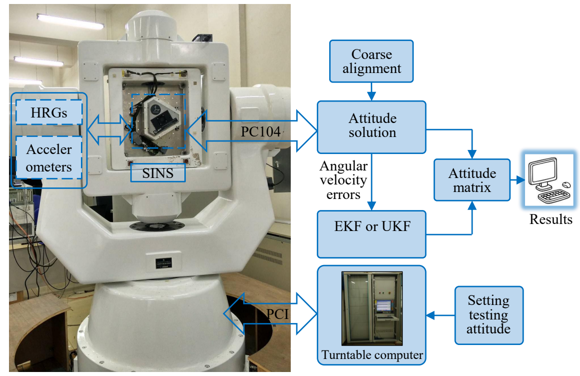

Fig. 5. Testing system of a redundant SINS.

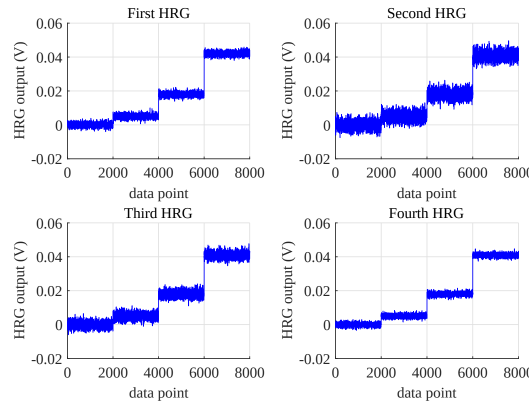

Fig. 6. Output of fault-free HRGs.

This paper mainly studies the large yaw misalignment angle in large misalignment angles. The main reasons causing the large yaw misalignment angle are the HRG zero bias fault and the accuracy of filtering algorithm.

A. Fault Diagnosis Results of Gyroscopes

First, the calibration experiment of each HRG is performed. The platform of a dual-axis position rate testing turntable is leveled; then, each HRG is fixed on the dual-axis turntable and the sensitive axis of the HRG coincides with the inner-ring axis of the turntable. The testing range of angular velocity is $-3°/\mathrm{s}$ to $+3°/\mathrm{s}$. HRGs are calibrated using an angular velocity test on the dual-axis turntable over 16 test points ($\pm 0.01°/\mathrm{s}$, $\pm 0.03°/\mathrm{s}$, $\pm 0.07°/\mathrm{s}$, $\pm 0.1°/\mathrm{s}$, $\pm 0.3°/\mathrm{s}$, $\pm 0.7°/\mathrm{s}$, $\pm 1°/\mathrm{s}$, and $\pm 3°/\mathrm{s}$). Each test point is sampled for 120s at 200Hz. Each calibration point generates $24,000$ samples (200Hz$\times$120s). The calibration of each HRG uses 16 points, resulting in $384,000$ samples. Thus, the input-output relationship of HRGs adopts a linear regression model [31]:

$$V_{gi} = K_{gi}\omega_i + V_{g0i} + \eta_{gi} \tag{46}$$

where ω_i is the input angular velocity of the ith HRG with the unit as $°/\mathrm{s}$, V_{gi} is the output voltage of the ith HRG with the unit as V, K_{gi} is the scale factor of the ith HRG with the unit as $\mathrm{V}/(°/\mathrm{s})$, V_{g0i} is the constant zero bias of the ith HRG with the unit as V, and η_{gi} is the fitting error with the unit as V. After testing, the HRG calibration results can be obtained by fitting with the least squares method (LSM),

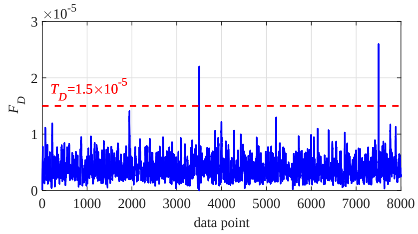

Fig. 7. F_D output of fault-free HRGs.

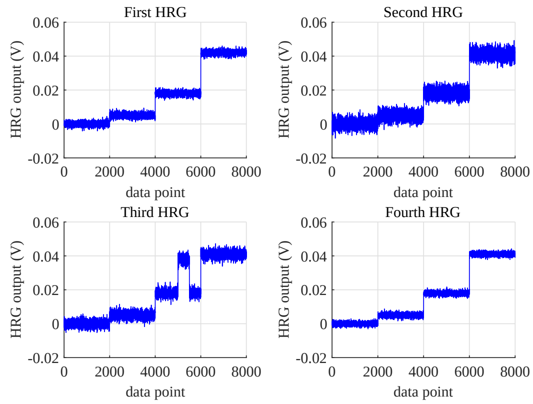

Fig. 8. Output of three operational HRGs and one malfunctioning HRG.

as shown in Table II. The linear regression models explicitly include a fitting error term η_{gi}, which encompasses HRG noise and unmodeled errors. In addition, their zero bias stability is also obtained through the root mean square error (RMSE) method.

Then, to verify the feasibility of the HRG fault diagnosis algorithm and determine the fault detection threshold, the following tests are carried out: four HRGs are installed in the position shown in Fig. 2. The turntable rotates at the angular velocities of $0.1°/\text{s}$, $0.3°/\text{s}$, $0.7°/\text{s}$, and $1°/\text{s}$, respectively. After the turntable's angular velocity is stable, the output voltages of HRGs are recorded. When the four HRGs are fault-free, the output is shown in Fig. 6. Based on the current HRG outputs, the fault detection index F_D of the HRGs can also be calculated, as shown in Fig. 7. According to (14), F_D follows a χ^2 distribution with the degree of freedom r, and the expected false alarm rate follows the 3τ principle, which means the false alarm rate is 0.27%. According to the data in Fig. 7, when the false alarm rate is 0.27%, $T_D = 1.5 \times 10^{-5}$. To simulate the fault, a bias of 0.02V is applied to the $5000 - 5500$ points of the third HRG, as shown in Fig. 8. The F_D output of HRGs after simulating the fault is shown in Fig. 9. The mean of the F_D output of the malfunctioning HRG at the $5000 - 5500$ points is 1.0005×10^{-4}, being much greater than T_D, which shows that faults can be effectively detected by applying the

TABLE II
HRG CALIBRATION RESULTS

HRG number	K_{gi} (V/(°/s))	V_{g0i} (V)	η_{gi} (V)	Zero bias stability (°/h)
1st	2.6413	0.0816	0.0138	0.0105
2nd	2.6144	0.0066	0.0035	0.0118
3rd	2.9222	0.0073	0.0347	0.0132
4th	2.8600	0.0317	0.0065	0.0126

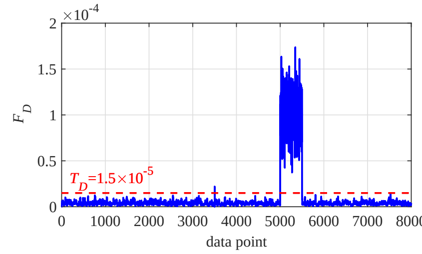

Fig. 9. F_D output of malfunctioning HRGs.

threshold T_D.

B. Comparative Results of SINS Initial Alignment Using Different Filtering Methods

After detecting whether there is a fault in the HRGs that causes a large yaw misalignment angle, the next step is to execute a filtering algorithm to achieve initial alignment of the large yaw misalignment angle. Firstly, the redundant SINS is calibrated using a three-axis turntable and aligned with the east-north-sky coordinate system. At this time, the real attitude angle is considered to be zero. After the SINS is started, the attitude error data is sampled for 300 seconds and repeated multiple times as the testing data for filters. Comparative experiments are conducted using EKF and UKF.

The initial conditions for the first group of SINS data are that initial pitch, roll, and yaw angle errors are $0.01°$, $0.01°$, and $1°$, respectively; after 300 seconds of alignment, the alignment error curve during filtering is shown in Fig. 10. The initial conditions for the second group of SINS data are that initial pitch, roll, and yaw angle errors are $0.01°$, $0.01°$, and $20°$ (large yaw misalignment angle), respectively; after 300 seconds of alignment, the alignment error curve is shown in Fig. 11. The initial conditions for the third group of SINS data are that initial pitch, roll, and yaw angle errors are $1°$, $1°$, and $1°$, respectively; the alignment error curve is shown in Fig. 12. The initial conditions for the fourth group of SINS data are that initial pitch, roll, and yaw angle errors are $1°$, $1°$, and $20°$ (large yaw misalignment angle), respectively; the alignment error curve is shown in Fig. 13. Comparative testing results of EKF and UKF filters in the initial alignment under large misalignment angles are shown in Table III. In the experiments, the approximate mean execution times per estimation cycle for the UKF and EKF are 130 and 100 microseconds, respectively. Thus, the mean execution time per estimation cycle for the UKF is approximately 1.3 times that of the EKF. This increase is attributable to the propagation of sigma points ($2n+1$ states) versus a single state. However, for the state dimension used in this alignment model ($n = 6-9$), the absolute difference is within 0.5 milliseconds on the embedded processor, well within the typical SINS update rate of 100Hz.

From Table III, it can be seen that the alignment accuracy of pitch and roll angles under two filter algorithms are almost the same, and UKF is slightly improved compared to EKF. The reason for this phenomenon is that the alignment accuracy of pitch and roll angles is limited by the performance of accelerometers. When the initial yaw misalignment angle is

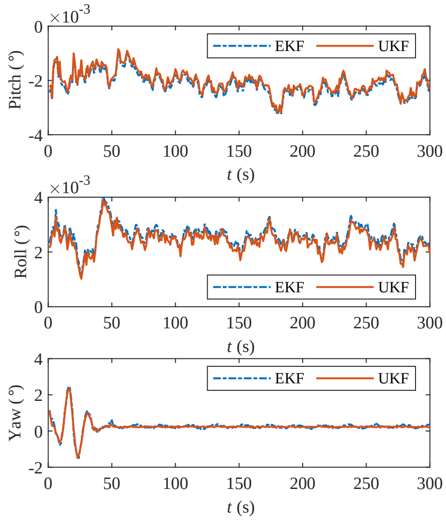

Fig. 10. Alignment error of the first group.

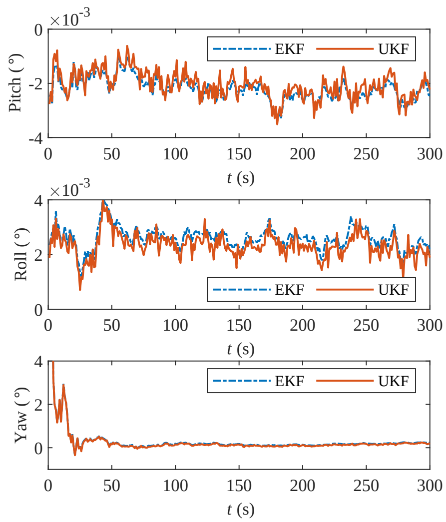

Fig. 11. Alignment error of the second group.

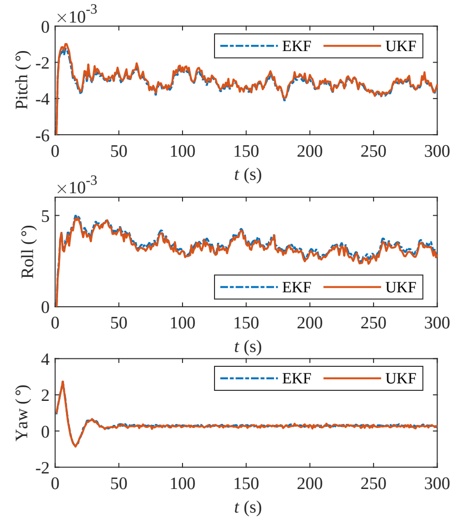

Fig. 12. Alignment error of the third group.

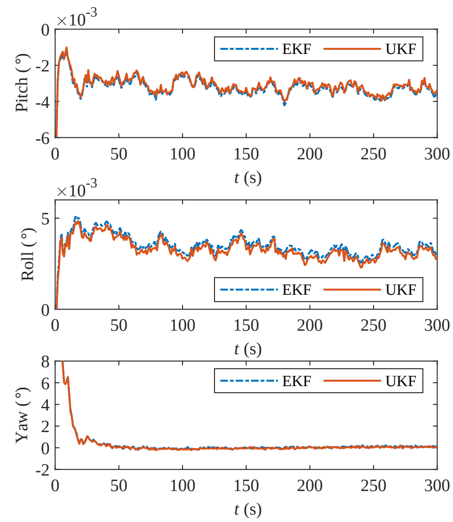

Fig. 13. Alignment error of the fourth group.

small, the alignment time and accuracy of two filter algorithms are comparable, which indicates that under the premise of the limited accuracy of inertial sensors, the alignment accuracy mainly depends on the rationality of the Gaussian assumption, and the mean and the integral calculation errors of covariance matrix become secondary factors. As the yaw misalignment angle increases, the alignment accuracy deteriorates. Especially, under the large yaw misalignment angle, the alignment accuracy of UKF is significantly improved compared to that of EKF. Based on the alignment error curves presented in Figs. 10 through 13, a convergence speed analysis is conducted based on the time required to reach 95% of the steady-state alignment error. Under a large yaw misalignment ($20°$), the UKF achieves stable convergence in approximately 200s, whereas the EKF fails to converge within the test duration of 300s. In contrast, for small yaw misalignment ($1°$), both filters converge within $100-150$s, which demonstrates comparable convergence speeds. These results indicate that the problem of large misalignment angles in initial alignment can be solved through gyroscope fault diagnosis and filtering algorithms.

In addition, the practical implications and limitations of the integrated framework (GLRT+UKF) are below. a) Computational load: The integrated framework is designed for real-time execution. While the UKF has a higher computational load than the EKF, the experiments confirm its feasibility on modern embedded processors within standard SINS update rates. The parity-based GLRT adds minimal overhead. b)

TABLE III
COMPARATIVE RESULTS OF INITIAL ALIGNMENT USING DIFFERENT FILTERS

Groups	Types	Pitch error ($°$)	Roll error ($°$)	Yaw error ($°$)	Convergence time (s)
First	EKF	0.0021	0.0026	0.2649	$\sim 100-120$s
	UKF	0.0020	0.0024	0.2411	$\sim 100-120$s
Second	EKF	0.0022	0.0026	0.3327	> 300s
	UKF	0.0021	0.0023	0.2997	$\sim 180-220$s
Third	EKF	0.0031	0.0034	0.3191	$\sim 120-150$s
	UKF	0.0030	0.0033	0.2905	$\sim 120-150$s
Fourth	EKF	0.0032	0.0035	0.3969	> 300s
	UKF	0.0031	0.0033	0.3466	$\sim 200-250$s

Scope of validation: A primary limitation is that the integrated framework is validated under static base conditions. Its performance in highly dynamic environments remains to be fully characterized. In such scenarios, the observability of errors changes, and additional adaptive mechanisms may be required.

V. Conclusion

This paper has successfully presented an integrated framework combining fault diagnosis and initial alignment for redundant SINSs operating under large misalignment angles. The proposed parity-based GLRT method proves effective for detecting and identifying gyroscope faults. The precise alignment employing an UKF effectively addresses the significant yaw error that analytic coarse alignment does not solve for the case of a large yaw misalignment angle. Comparative experiments confirm that the UKF's performance is comparable to the EKF for small misalignment angles but becomes distinctly superior when confronting large yaw misalignment angles. Thus, the synergy of a fault-tolerant sensor configuration and a sophisticated nonlinear filtering strategy provides a practical and high-precision solution, which significantly improves alignment accuracy and system reliability under adverse initial conditions. In the future, further researches are to extend the validation to moving-base alignment and potentially enhance the UKF with adaptive noise estimation or robust integration techniques.

References

[1] Z. Wang, X. Lun, Y. Jiang, and H. Luo, "Fault-tolerant sun-pointing attitude control based on physics-guided neural networks," *IEEE Trans. Ind. Inf.*, vol. 20, no. 12, pp. 13 956–13 965, 2024.

[2] Z. Xu, B. Xi, G. Yi, and C. K. Ahn, "High-precision control scheme for hemispherical resonator gyroscopes with application to aerospace navigation systems," *Aero. Sci. Technol.*, vol. 119, pp. 1–11, 2021, Art no. 107168.

[3] X. Xu, Z. Guo, Y. Yao, and T. Zhang, "Robust initial alignment for SINS/DVL based on reconstructed observation vectors," *IEEE/ASME Trans. Mechatron.*, vol. 25, no. 3, pp. 1659–1667, 2020.

[4] H. G. Wang and T. C. Williams, "Strategic inertial navigation systems - high-accuracy inertially stabilized platforms for hostile environments," *IEEE Control Syst. Mag.*, vol. 28, no. 1, pp. 65–85, 2008.

[5] Y. Jiang and S. Yin, "Recursive total principle component regression based fault detection and its application to vehicular cyber-physical systems," *IEEE Trans. Ind. Inf.*, vol. 14, no. 4, pp. 1415–1423, 2018.

[6] Q. Zhang, Q. Chen, Z. Xu, T. Zhang, and X. Niu, "Evaluating the navigation performance of multi-information integration based on low-end inertial sensors for precision agriculture," *Precision Agric.*, vol. 22, pp. 627–646, 2021.

[7] Y. Wu, X. Hu, D. Hu, T. Li, and J. Lian, "Strapdown inertial navigation system algorithms based on dual quaternions," *IEEE Trans. Aero. Electron. Syst.*, vol. 41, no. 1, pp. 110–132, 2005.

[8] M. Bai, Y. Huang, Y. Zhang, and F. Chen, "A novel heavy-tailed mixture distribution based robust Kalman filter for cooperative localization," *IEEE Trans. Ind. Inf.*, vol. 17, no. 5, pp. 3671–3681, 2021.

[9] Z. Xu, Y. Wang, Z. Wu, W. X. Zheng, and C. Hu, "Federated learning-based offset-free distributed control of nonlinear networked systems with application to IIoT," *IEEE Trans. Netw. Sci. Eng.*, vol. 12, no. 3, pp. 1859–1871, 2025.

[10] S. Zhang, T. Zhang, S. Li, L. Zhang, and Y. Shi, "A novel underwater SINS/USBL dual-responder integrated navigation algorithm considering motion effects," *IEEE Trans. Instrumen. Meas.*, vol. 74, pp. 1–13, 2025, Art no. 9525213.

[11] H. Wei, T. Zhang, L. Zhang, and L. Zhong, "Point-state segmentation for dynamic scenes via probability model and orientation consistency," *IEEE Trans. Ind. Inf.*, vol. 20, no. 6, pp. 8428–8440, 2024.

[12] J. Jia, Z. Song, S. Gao, Y. Gao, and H. Cao, "Bandwidth expansion for force-to-rebalance measurement of MEMS gyroscopes based on equivalent unit negative feedback loop," *IEEE/ASME Trans. Mechatron.*, vol. 30, no. 6, pp. 4613–4624, 2025.

[13] M. Bai, Y. Huang, Y. Zhang, and J. Chambers, "Statistical similarity measure-based adaptive outlier-robust state estimator with applications," *IEEE Trans. Autom. Control*, vol. 67, no. 8, pp. 4354–4361, 2022.

[14] J. Liu, X. Chen, and J. Wang, "Strong tracking UKF-based hybrid algorithm and its application to initial alignment of rotating SINS with large misalignment angles," *IEEE Trans. Ind. Electron.*, vol. 70, no. 8, pp. 8334–8343, 2023.

[15] J. Lu, L. Xie, and B. Li, "Applied quaternion optimization method in transfer alignment for airborne AHRS under large misalignment angle," *IEEE Trans. Instrumen. Meas.*, vol. 65, no. 2, pp. 346–354, 2016.

[16] R. Cui, W. Wei, Q. Cai, C. Shen, and H. Cao, "A thermal-robust bandwidth expansion method for MEMS gyroscopes based on parameter self-adjustment," *IEEE Trans. Instrumen. Meas.*, vol. 74, pp. 1–9, 2025, Art no. 9529609.

[17] D. H. Titterton and J. L. Weston, *Strapdown Inertial Navigation Technology*, 2nd ed. Stevenage, UK: Institution of Engineering and Technology, 2004.

[18] H. Shao, L. Miao, W. Gao, and J. Shen, "Ensemble particle filter based on KLD and its application to initial alignment of the SINS in large misalignment angles," *IEEE Trans. Ind. Electron.*, vol. 65, no. 11, pp. 8946–8955, 2018.

[19] Y. Yang, D. Li, Y. Fu, and K. Xu, "Strong tracking dimensionality-reduction CKF algorithm for SINS initial alignment under large misalignment angle," *Sci. Rep.*, vol. 15, pp. 1–17, 2025, Art no. 34535.

[20] W. Zou, Q. Fu, and Z. Wen, "A transfer alignment algorithm based on grading correction with large misalignment angle," *IEEE Trans. Instrumen. Meas.*, vol. 74, pp. 1–11, 2025, Art no. 8504111.

[21] L. Wang and Y. Xia, "Mars entry navigation with uncertain parameters based on desensitized extended Kalman filter," *IEEE Trans. Ind. Inf.*, vol. 11, no. 5, pp. 998–1005, 2015.

[22] B. Zhu, J. Li, G. Cui, W. Shi, and X. Guo, "Robust initial alignment based on unscented information Kalman filter," *IEEE Sensors J.*, vol. 22, no. 21, pp. 21 024–21 034, 2022.

[23] I. Arasaratnam, S. Haykin, and T. R. Hurd, "Cubature Kalman filtering for continuous-discrete systems: Theory and simulations," *IEEE Trans. Signal Process.*, vol. 58, no. 10, pp. 4977–4993, 2010.

[24] B. Jia, M. Xin, and Y. Cheng, "Anisotropic sparse Gauss-Hermite quadrature filter," *J. Guidance Control Dynamics*, vol. 35, no. 3, pp. 1014–1023, 2012.

[25] J. Ali and M. Nzar, "Realization of initial alignment algorithm for strapdown inertial navigation system using central difference filter," *IFAC Proc. Vol.*, vol. 41, no. 2, pp. 4731–4736, 2008, 17th IFAC World Congress.

[26] Z. Xu, S. S. Ge, W. Liu, G. Yi, Z. Xie, and K. Li, "Intermittently dynamic fuzzy learning-based tracking control of amplitude signals for vibratory gyroscopes with composite identification," *IEEE Trans. Instrumen. Meas.*, vol. 74, pp. 1–8, 2025, Art no. 9518508.

[27] Z. Xu, D. Wang, G. Yi, and Z. Hu, "Asynchronous tracking control of amplitude signals in vibratory gyroscopes with partially unknown mode information," *IEEE Trans. Ind. Electron.*, vol. 70, no. 7, pp. 7478–7487, 2023.

[28] J. V. Harrison and E. G. Gai, "Evaluating sensor orientations for navigation performance and failure detection," *IEEE Trans. Aero. Electron. Syst.*, vol. 13, no. 6, pp. 631–643, 1977.

[29] Y. Jiang, S. Yin, and O. Kaynak, "Optimized design of parity relation-based residual generator for fault detection: Data-driven approaches," *IEEE Trans. Ind. Inf.*, vol. 17, no. 2, pp. 1449–1458, 2021.

[30] S. Wang and H. Zhang, "Fault detection threshold determination in a redundant strapdown inertial navigation system," *Acta Aero. et Astro. Sinica*, vol. 21, no. 4, pp. 303–307, 2000.

[31] Z. Xu, G. Yi, and W. Zhu, "An accurate thermoelastic model and thermal output error analysis of a hemispherical resonator gyroscope under varying temperatures," *Mecha. Syst. Signal Processing*, vol. 170, pp. 1–18, 2022, Art no. 108760.